LETTER

doi:10.1038/nature10290

Microwave quantum logic gates for trapped ions

C. Ospelkaus[1]†, U. Warring[1], Y. Colombe[1], K. R. Brown[1]†, J. M. Amini[1]†, D. Leibfried[1] & D. J. Wineland[1]

Control over physical systems at the quantum level is important in fields as diverse as metrology, information processing, simulation and chemistry. For trapped atomic ions, the quantized motional and internal degrees of freedom can be coherently manipulated with laser light[1,2]. Similar control is difficult to achieve with radio-frequency or microwave radiation: the essential coupling between internal degrees of freedom and motion requires significant field changes over the extent of the atoms' motion[2,3], but such changes are negligible at these frequencies for freely propagating fields. An exception is in the near field of microwave currents in structures smaller than the free-space wavelength[4,5], where stronger gradients can be generated. Here we first manipulate coherently (on time-scales of 20 nanoseconds) the internal quantum states of ions held in a microfabricated trap. The controlling magnetic fields are generated by microwave currents in electrodes that are integrated into the trap structure. We also generate entanglement between the internal degrees of freedom of two atoms with a gate operation[4,6–8] suitable for general quantum computation[9]; the entangled state has a fidelity of 0.76(3), where the uncertainty denotes standard error of the mean. Our approach, which involves integrating the quantum control mechanism into the trapping device in a scalable manner, could be applied to quantum information processing[4], simulation[5,10] and spectroscopy[3,11].

The quantized mechanical motion and internal states of trapped atoms can be coherently controlled by laser radiation. This optical control has led to the creation of non-classical motional states[1–3], multiparticle entanglement[1], scalable quantum logic techniques[12], quantum simulation studies[13–15] and quantum logic spectroscopy[11]. The coupling between internal and motional states is provided by the gradient of the driving field over the extent, Δx, of the atoms' motion[2,3]. For trapped atomic ions in their lowest motional quantum levels, $\Delta x \approx 10$ nm, which is a significant fraction of an optical wavelength, resulting in an efficient coupling between motional and internal states. A microwave field propagating in free space varies only very slightly over Δx, and the corresponding coupling between motional and internal states is highly suppressed.

Notwithstanding the success of laser-based control, it is desirable to develop a microwave approach with equivalent capabilities because of the relative ease of generating and controlling these fields. One method uses a combination of uniform microwave fields and static, state-dependent potentials to provide motional–internal state coupling[16–19] and individual addressing[18,20]. Related to this are magnetic microwave or radio-frequency-dressed state potentials for neutral atoms[21]. Here we implement the approach outlined in ref. 4, where the magnetic field from oscillating microwave currents in trap electrodes provides coherent manipulation of the internal state, and the gradient of this field leads to motional–internal state coupling. These interactions suffice for universal quantum information processing, because any unitary operation on quantum bits (qubits) can be decomposed into a sequence of single-qubit rotations and a suitable entangling interaction[9]. By comparison with laser-based approaches, microwave control has the potential to improve significantly the fidelity of operations owing to its reduced sensitivity to 'spectator modes' of ion motion[3], its better control of field amplitudes and phases, and the absence of spontaneous-emission decoherence[4,16]. Furthermore, microwave near-field control could be incorporated in a chip-level library of transport, junction, storage and microwave manipulation components[22] to advance the integration of quantum control in scalable quantum information processing or simulation.

Our apparatus comprises a room-temperature (300 K) surface-electrode ion trap[23] with 10-μm-thick gold electrodes, separated by gaps of 4.5 μm, deposited onto an insulating AlN substrate (Fig. 1). An oscillating potential (amplitude, 25–50 V; frequency, $f_{RF} = 70.97$ MHz), applied to the radio-frequency electrodes (Fig. 1, RF1 and RF2), provides pseudopotential confinement of $^{25}Mg^{+}$ ions in the radial (x and z) directions at a distance of 30 μm from the electrode surface (all other electrodes are held at radio-frequency ground). Along the trap y axis, ions are confined with static potentials applied to control electrodes C1, C3, C4 and C6. The radial field resulting from these potentials is compensated for by suitable potentials applied to electrodes C2 and C5. Single-ion oscillation frequencies along the y direction can be adjusted between 300 kHz and 2 MHz, and radial frequencies can be adjusted between 4 and 10 MHz. Microwave electrodes MW1, MW2 and MW3 support currents, of order 100 mA to 1 A, that produce an oscillating magnetic field, $\mathbf{B}_{osc}$, above the surface and are used to implement quantum control. To minimize thermal effects during these microwave pulses, we chose AlN as the electrode substrate. It provides a strong thermal link between the gold electrodes and a solid copper support through a thin layer of vacuum-compatible epoxy. A static magnetic field, $\mathbf{B}_0$, parallel to the trap surface and at an angle of 15° with respect to the z axis, provides the internal-state quantization axis. Superimposed circularly (σ^{-})-polarized laser beams nearly resonant

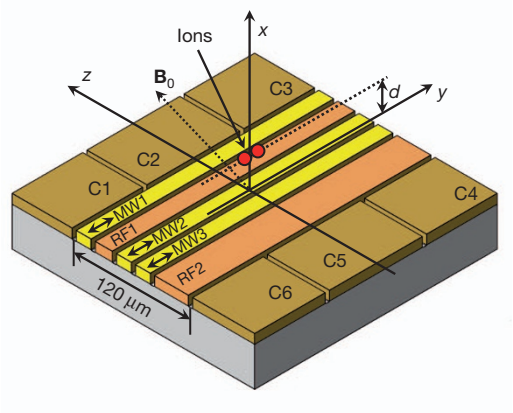

Figure 1 | Central portion of the surface-electrode trap. The control electrodes are labelled C1 to C6, trap radio-frequency electrodes are labelled RF1 and RF2, and microwave lines are labelled MW1 to MW3. The ions are held a distance $d = 30$ μm above the surface. By comparison with the symmetric trap structure of ref. 4, the asymmetric geometry of the microwave and radio-frequency electrodes used here yields approximately equal microwave currents in all three electrodes for field suppression at the ions while providing a deeper trap.

[1]Time and Frequency Division, National Institute of Standards and Technology, 325 Broadway, Boulder, Colorado 80305, USA. †Present addresses: Institute of Quantum Optics, Leibniz Universität Hannover, Welfengarten 1, 30167 Hannover, and PTB, Bundesallee 100, 38116 Braunschweig, Germany (C.O.); GTRI Georgia Tech, 400 10th Street NW, Atlanta, Georgia 30318, USA (K.R.B., J.M.A.).

with $3^2S_{1/2} \rightarrow 3^2P_{3/2}$ transitions and propagating parallel to $\mathbf{B}_0$ are used for optical pumping, Doppler laser cooling and state detection through resonance fluorescence. Optical pumping prepares ions in the $|F = 3, m_F = -3\rangle$ hyperfine ground state. Using microwave pulses resonant with hyperfine transitions, we can prepare an arbitrary pure state within the ground-state manifold (Fig. 2a) with fidelity greater than 0.98 (Methods). Furthermore, we can detect the population in any one of these states by applying a series of microwave π-pulses to transfer its population to $|3, -3\rangle$ and then detecting resonance fluorescence on the $|3, -3\rangle \rightarrow |3^2P_{3/2}, F = 4, m_F = -4\rangle$ optical cycling transition.

At a bias field of $B_0 \approx 21.3$ mT, we realize a first-order magnetic-field-independent transition between the qubit states $|3, 1\rangle \equiv |\downarrow\rangle$ and $|2, 1\rangle \equiv |\uparrow\rangle$ with 'carrier' frequency $f_0 \approx 1.69$ GHz (Fig. 2a, solid line). To prepare $|\downarrow\rangle$, after optically pumping the ions to $|3, -3\rangle$, we apply four microwave π-pulses (Fig. 2a, dotted lines). Figure 2b shows Ramsey spectroscopy measurements of the $|\downarrow\rangle \rightarrow |\uparrow\rangle$ transition frequency as a function of magnetic field detuning, δB, from B_0. At $\delta B = 0$, the transition frequency depends on δB only to second order, a feature that has been shown to allow long coherence times (~10 s) despite moderate ambient magnetic field noise[24].

Rabi flopping on the $|\downarrow\rangle \rightarrow |\uparrow\rangle$ transition with a complete state exchange time (π-time) of 18.63(3) ns (Fig. 2c) demonstrates the speed of single-qubit operations. This is more than 200 times shorter than a typical π-time (4 μs) obtained with continuous-wave Raman laser beams[25]. Moreover, it is nine orders of magnitude shorter than the coherence time achieved on a similar field-independent transition[24]. (For very short π-pulses realized with pulsed lasers, see ref. 26.)

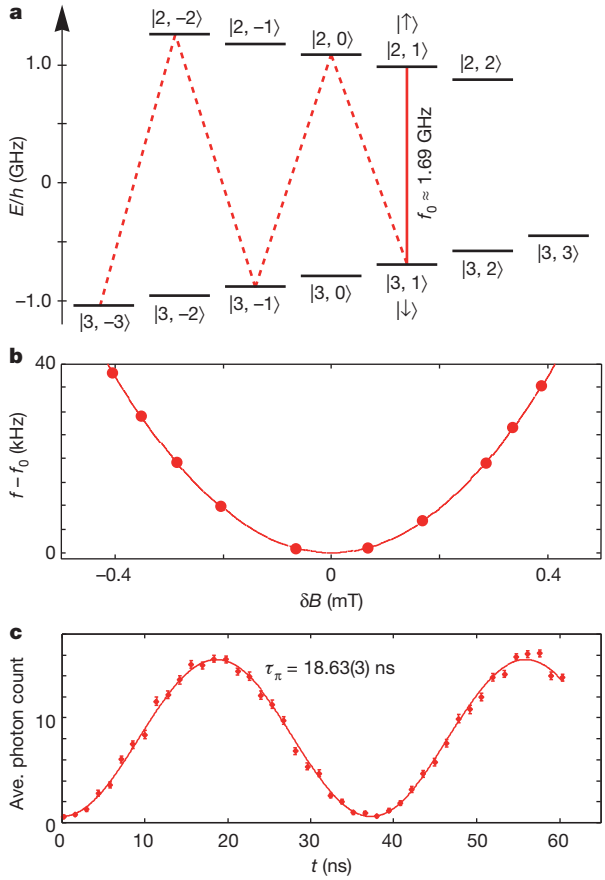

Figure 2 | Level scheme of $^{25}Mg^+$ (nuclear spin, $I = 5/2$) and spectroscopy of the qubit transition. **a**, Ground-state hyperfine structure of $^{25}Mg^+$ at $B_0 \approx 21.3$ mT and the microwave transitions used in the experiment. *h*, Planck's constant. **b**, Frequency of the $|\downarrow\rangle \leftrightarrow |\uparrow\rangle$ transition as a function of bias-field detuning, δB, from the field-independent point, B_0. The standard errors of the measured frequencies are less than 5 Hz. **c**, Rabi flopping on the $|\downarrow\rangle \leftrightarrow |\uparrow\rangle$ transition induced by microwave current in MW2, the electrode in closest proximity to the ions. Error bars, s.e.m. for the average photon count in 400 μs. τ_π, π-time.

To achieve coupling between motional and internal states, we apply sufficiently large oscillating magnetic field gradients at frequencies $f_s \approx f_0 \pm f_r$ near the motional sidebands of the qubit transition carrier frequency, f_0 (where f_r is a radial motional-mode frequency). At the same time, we want to suppress $\mathbf{B}_{osc}$ at the ions because it can cause undesirable off-resonant carrier excitation and a.c. Zeeman shifts, analogous to a.c. Stark shifts for optical fields[4]. In the geometry of Fig. 1, there is a single combination of relative current amplitudes and phases in electrodes MW1, MW2 and MW3 that provides an oscillating magnetic field gradient at the ions without an oscillating magnetic field.

We find this combination by adjusting the amplitudes and phases of the currents to minimize the a.c. Zeeman shifts on the qubit and neighbouring hyperfine transitions. To characterize the resulting field, we map the *x*–*z* spatial dependence of the a.c. Zeeman shift on a selected magnetic dipole hyperfine transition by displacing the ion radially from its nominal position with adjustments of the static trap potentials. Within a small region around the oscillating field zero, we expect $\mathbf{B}_{osc}$ to be a quadrupole characterized by a gradient strength, B', and an angle, α (the angle of one principal axis of the quadrupole with respect to the *x* axis; see Methods). A fit based on this model and to the experimental a.c. Zeeman shift data yields $B' = 35.3(4)\,\mathrm{T\,m^{-1}}$ and $\alpha = 26.6(7)^\circ$. For comparison, a plane-wave microwave field with the amplitude required to produce the π-time of Fig. 2c (1.9 mT), has a gradient of only $0.068\,\mathrm{T\,m^{-1}}$. Knowledge of the orientation and gradient of the field can be used to predict sideband Rabi rates and to optimize the overlap with one of the radial motional modes. From the measured gradient and the assumption of optimal alignment of the mode with the gradient, we calculate a sideband π-time[4] of approximately 190 μs at a motional frequency of 6.5 MHz for a single ion in its motional ground state (Methods).

After approximately optimizing the field configuration, we implemented motional sideband transitions on one ion and on a pair of ions. As an example of a two-ion sideband application, we perform the following experiments on the selected radial rocking mode. First, two ions are Doppler-cooled and prepared in the $|\uparrow\uparrow\rangle$ state. We then apply a qubit π-pulse followed by a sideband pulse at $f_s = f_0 + f_r$ (here $f_r \approx 6.8$ MHz for the chosen rocking mode). The sideband pulse induces transitions from $|\downarrow\downarrow, n\rangle$ to $|\uparrow\downarrow, n+1\rangle$, $|\downarrow\uparrow, n+1\rangle$ and $|\uparrow\uparrow, n+2\rangle$, where n denotes the motional quantum number[27]. Populations in $|\downarrow\rangle$ are subsequently transferred to $|3, -3\rangle$ and detected by laser fluorescence. In Fig. 3a (blue circles), we show the result of a frequency scan of the sideband pulse. We then repeat the above experiment, but swap the order of the sideband pulse and the carrier π-pulse (Fig. 3a, red squares). In this case, the sideband pulse drives transitions from $|\uparrow\uparrow, n\rangle$ to $|\downarrow\uparrow, n-1\rangle$, $|\uparrow\downarrow, n-1\rangle$ and $|\downarrow\downarrow, n-2\rangle$. If we assume a thermal motional state (valid for Doppler cooling), a fit to the data gives an average occupation number of $\bar{n} = 2.2(1)$.

Multiple sideband cooling cycles can be used to cool a selected motional mode to near the ground state[2,27]. One sideband cooling cycle consists of transitions from $|\uparrow\uparrow, n\rangle$ to $|\downarrow\uparrow, n-1\rangle$, $|\uparrow\downarrow, n-1\rangle$ and $|\downarrow\downarrow, n-2\rangle$, where the pulse duration (250 μs) is optimized for maximal sideband asymmetry. This is followed by a repumping laser pulse resonant with the $|\downarrow\rangle \rightarrow |3^2P_{3/2},\ m_J = -3/2,\ m_I = 3/2\rangle$ transition (where m_J and m_I are the components of the total electronic and nuclear angular momenta parallel to the static magnetic field, $\mathbf{B}_0$). From the relevant Clebsch–Gordan coefficients, we predict a 97% repumping efficiency to $|\uparrow\rangle$ after scattering 20 photons on average. Figure 3b shows a frequency scan of the motion-adding and motion-subtracting sidebands after four sideband cooling cycles. Assuming an approximately thermal distribution after cooling[27], we find that $\bar{n} = 0.6(1)$, confirming the sideband cooling. Lower temperatures could not be achieved by adding more cooling cycles, and the final

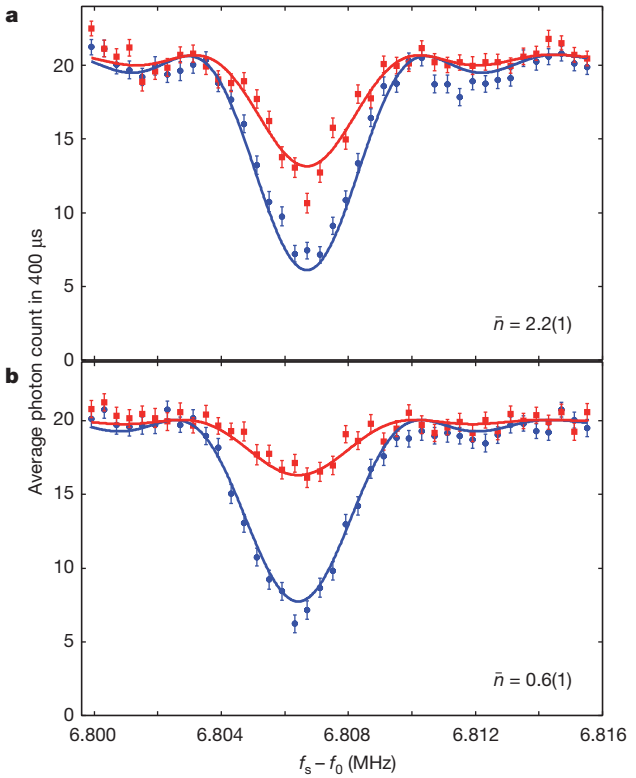

Figure 3 | Microwave motional sideband transitions. **a**, Motion-subtracting $|\uparrow\uparrow, n\rangle \rightarrow \{|\uparrow\downarrow, n-1\rangle, |\downarrow\uparrow, n-1\rangle, |\downarrow\downarrow, n-2\rangle\}$ (red squares) and motion-adding $|\downarrow\downarrow, n\rangle \rightarrow \{|\uparrow\downarrow, n+1\rangle, |\downarrow\uparrow, n+1\rangle, |\uparrow\uparrow, n+2\rangle\}$ (blue circles) sideband transitions for a Doppler-cooled two-ion radial rocking mode. **b**, Sideband transitions after four sideband cooling cycles. Error bars, s.e.m. for the average photon count in 400 μs.

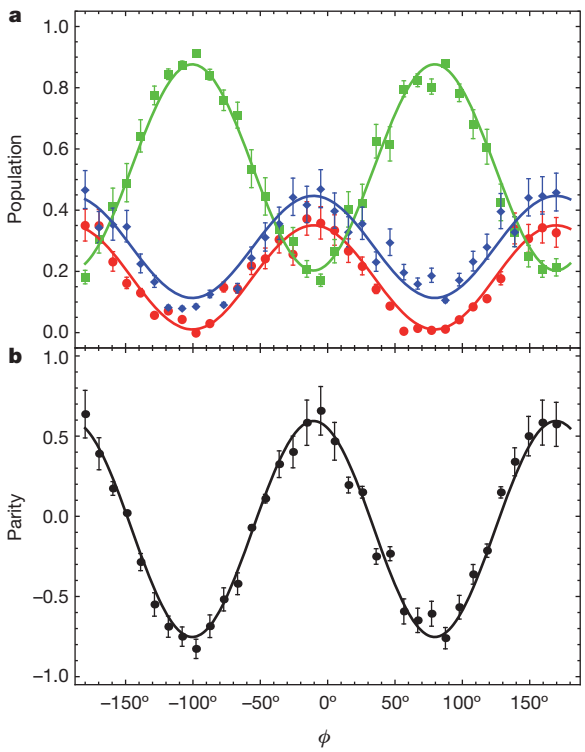

Figure 4 | Populations and parity of the entangled state. After the entanglement operation is applied to the $|\downarrow\downarrow\rangle$ state, an analysis π/2-pulse with relative phase ϕ is applied. Ideally, as ϕ is varied, $|\Psi\rangle$ is transformed into superpositions of $|\Psi\rangle$ and $(1/\sqrt{2})(|\uparrow\downarrow\rangle + |\downarrow\uparrow\rangle)$, and parity and populations of the two ions oscillate at $\cos(2\phi + \phi_0)$. **a**, Populations in $|\uparrow\uparrow\rangle$ ($P_{|\uparrow\uparrow\rangle}$, red disks), $|\downarrow\downarrow\rangle$ ($P_{|\downarrow\downarrow\rangle}$, blue diamonds) and $|\uparrow\downarrow\rangle$ plus $|\downarrow\uparrow\rangle$ ($P_{|\uparrow\downarrow\rangle} + P_{|\downarrow\uparrow\rangle}$, green squares). **b**, Parity $\Pi = (P_{|\uparrow\uparrow\rangle} + P_{|\downarrow\downarrow\rangle}) - (P_{|\uparrow\downarrow\rangle} + P_{|\downarrow\uparrow\rangle})$. Each data point represents an average of 300 experiments. We determine an entangled-state fidelity of $F_s = 0.76(3)$ from the populations in **a**. Error bars, s.e.m. for the populations and parity.

value of $\bar{n}$ was most probably limited by the repumping photon recoil and by heating from ambient electric field noise[27] during the course of the sequence. Separately, we measured the relevant motional heating rate and found it to be as low as $d\bar{n}/dt = 0.2\ \mathrm{ms}^{-1}$ at $f_r = 7.7$ MHz; however, higher heating rates were also observed. We did not detect additional heating induced by the microwave pulses.

Simultaneous application of two field gradients at $f_0 \pm (f_r + \delta)$, with $\delta \ll f_r$, is used to implement an entangling two-qubit gate[4]. By comparison with light fields, derivatives of the microwave fields of order higher than linear have negligible effect on the ions[4], so the ions are only Doppler-cooled and prepared in the $|\downarrow\downarrow\rangle$ state. We then apply the two oscillating field gradients with $f_r = 7.6$ MHz (rocking mode) and $\delta = 4.9$ kHz. To suppress decoherence caused by motional frequency instability, we apply the fields in two pulses of duration 200 μs, reversing the phase of one field in the second pulse[28]. For properly chosen pulse durations, the internal states ideally end in the entangled state $|\Psi\rangle = (1/\sqrt{2})(|\downarrow\downarrow\rangle - i|\uparrow\uparrow\rangle)$, with the motion restored to the state it was in before the gate operation[6]. Pulse imperfections and decoherence during the operation produce a mixed state with density matrix ρ (after tracing over the motion). We characterize the fidelity of ρ with respect to the ideal outcome, $F_s = \langle\Psi|\rho|\Psi\rangle = (1/2)(\rho_{\uparrow\uparrow,\uparrow\uparrow} + \rho_{\downarrow\downarrow,\downarrow\downarrow}) + |\rho_{\uparrow\uparrow,\downarrow\downarrow}|$, by observing population oscillations as we sweep the phase, ϕ, of a π/2-pulse applied to the qubits after creating the entangled state[29]. The populations $\rho_{\downarrow\downarrow,\downarrow\downarrow}$, $\rho_{\uparrow\downarrow,\uparrow\downarrow} + \rho_{\downarrow\uparrow,\downarrow\uparrow}$ and $\rho_{\uparrow\uparrow,\uparrow\uparrow}$ can be directly determined by fitting histograms for two, one or zero fluorescing ions to the histograms of the total fluorescence signal obtained during the sweep (Methods). The resulting populations are shown in Fig. 4a. The magnitude of the density matrix element $\rho_{\uparrow\uparrow,\downarrow\downarrow}$ is equal to the amplitude, A_Π, of the parity $\Pi = (P_{|\uparrow\uparrow\rangle} + P_{|\downarrow\downarrow\rangle}) - (P_{|\uparrow\downarrow\rangle} + P_{|\downarrow\uparrow\rangle})$, which oscillates like $A_\Pi \cos(2\phi + \phi_0)$ (ref. 29; Fig. 4b). By fitting sinusoids to the observed populations, we extract a fidelity of $F_s = 0.76(3)$ with respect to the state $|\Psi\rangle$.

For scalable implementations of quantum information processing, the quality of all operations demonstrated here, in particular that of the entangling operation, must be improved considerably. This will require significant technical improvements; however, there are no apparent fundamental limits to fidelity. The most important factors currently limiting two-qubit gate fidelity are the stability of motional frequencies in the trap and the precision with which we can suppress $\mathbf{B}_{osc}$ at the positions of the ions. Fluctuations of the motional frequencies are of the order of 1 kHz during the gate, which is a sizeable fraction of the gate detuning, δ, and seem to be primarily caused by time-varying stray potentials on the trap chip. It should be possible to suppress such stray fields by improving the surface quality of the electrodes, by reducing the amount of nearby dielectric material (dust and the residue of materials used during fabrication), by more carefully cleaning the electrode surfaces and by minimizing the exposure of the electrodes to ultraviolet light, which can generate charge through photoemission. We are able to suppress the oscillating field at the positions of the ions to fluctuations with amplitudes of approximately 10 μT, implying an a.c. Zeeman shift of less than 1 kHz. These fluctuations could be further suppressed by improving the amplitude stability and shaping of the microwave pulses and by using more sophisticated microwave current leads.

The presence of many processing zones on the same chip can introduce cross-talk between zones. Cross-talk for two-qubit gates can be suppressed by choosing substantially different mode frequencies for qubits in nearby 'spectator' trap zones. For single-qubit rotations, it should be possible to reduce the field to near zero in spectator zones by applying local compensating fields. Composite pulse techniques can also prove useful in enhancing spectator-zone isolation[30]. Traps smaller

than those used here should lead to faster operations[4], provided that anomalous motional heating can be suppressed. Multi-ion operations similar to those demonstrated here might also be used for quantum simulation[5,10], possibly with less stringent requirements on suppression of cross-talk. For particles lacking the electronic structure needed for laser manipulation and read-out, microwave sidebands would allow excitation of the motion conditioned on the internal-state magnetic moment[31]. The presence of the motional excitation could then be observed with an ancilla ion, either through a shared motional mode[11] or through the Coulomb interaction between ions held in separate traps[3,31–33]. In the second case, this technique might allow a comparison of the proton and antiproton magnetic moments[3,31].

METHODS SUMMARY

We describe the oscillating magnetic field geometry in the vicinity of the ions, and the experimental determination of this geometry, by mapping out a.c. Zeeman shifts experienced by the ions as functions of their positions. See the Methods for more details. There we also explain how state populations are extracted from fluorescence measurements to derive the fidelity of the entangled state produced by the two-qubit gate.

Full Methods and any associated references are available in the online version of the paper at www.nature.com/nature.

Received 13 April; accepted 14 June 2011.

1. Blatt, R. & Wineland, D. J. Entangled states of trapped atomic ions. *Nature* **453,** 1008–1015 (2008).
2. Leibfried, D., Blatt, R., Monroe, C. & Wineland, D. J. Quantum dynamics of single trapped ions. *Rev. Mod. Phys.* **75,** 281–324 (2003).
3. Wineland, D. J. *et al.* Experimental issues in coherent quantum-state manipulation of trapped atomic ions. *J. Res. Natl Inst. Stand. Technol.* **103,** 259–328 (1998).
4. Ospelkaus, C. *et al.* Trapped-ion quantum logic gates based on oscillating magnetic fields. *Phys. Rev. Lett.* **101,** 090502 (2008).
5. Chiaverini, J. & Lybarger, W. E. Laserless trapped-ion quantum simulations without spontaneous scattering using microtrap arrays. *Phys. Rev. A* **77,** 022324 (2008).
6. Sørensen, A. & Mølmer, K. Quantum computation with ions in thermal motion. *Phys. Rev. Lett.* **82,** 1971–1974 (1999).
7. Solano, E., de Matos Filho, R. L. & Zagury, N. Deterministic Bell states and measurement of the motional state of two trapped ions. *Phys. Rev. A* **59,** R2539–R2543 (1999).
8. Milburn, G. J., Schneider, S. & James, D. F. V. Ion trap quantum computing with warm ions. *Fortschr. Phys.* **48,** 801–810 (2000).
9. Barenco, A. *et al.* Elementary gates for quantum computation. *Phys. Rev. A* **52,** 3457–3467 (1995).
10. Schmied, R., Wesenberg, J. H. & Leibfried, D. Optimal surface-electrode trap lattices for quantum simulation with trapped ions. *Phys. Rev. Lett.* **102,** 233002 (2009).
11. Schmidt, P. O. *et al.* Spectroscopy using quantum logic. *Science* **309,** 749–752 (2005).
12. Knoop, M. Hilico, L. & Eschner, J. (eds) *Modern Applications of Trapped Ions* (J. Phys. B Vol. 42, Institute of Physics, 2009).
13. Porras, D. & Cirac, J. I. Effective quantum spin systems with trapped ions. *Phys. Rev. Lett.* **92,** 207901 (2004).
14. Friedenauer, A., Schmitz, H., Glueckert, J. T., Porras, D. & Schaetz, T. Simulating a quantum magnet with trapped ions. *Nature Phys.* **4,** 757–761 (2008).
15. Kim, K. *et al.* Quantum simulation of frustrated Ising spins with trapped ions. *Nature* **465,** 590–593 (2010).
16. Mintert, F. & Wunderlich, C. Ion-trap quantum logic using long-wavelength radiation. *Phys. Rev. Lett.* **87,** 257904 (2001).
17. Ciaramicoli, G., Marzoli, I. & Tombesi, P. Scalable quantum processor with trapped electrons. *Phys. Rev. Lett.* **91,** 017901 (2003).
18. Johanning, M. *et al.* Individual addressing of trapped ions and coupling of motional and spin states using RF radiation. *Phys. Rev. Lett.* **102,** 073004 (2009).
19. Förster, L. *et al.* Microwave control of atomic motion in optical lattices. *Phys. Rev. Lett.* **103,** 233001 (2009).
20. Wang, S. X., Labaziewicz, J., Ge, Y., Shewmon, R. & Chuang, I. L. Individual addressing of ions using magnetic field gradients in a surface-electrode ion trap. *Appl. Phys. Lett.* **94,** 094103 (2009).
21. Fortágh, J. & Zimmermann, C. Magnetic microtraps for ultracold atoms. *Rev. Mod. Phys.* **79,** 235–289 (2007).
22. Amini, J. M. *et al.* Toward scalable ion traps for quantum information processing. *New J. Phys.* **12,** 033031 (2010).
23. Seidelin, S. *et al.* Microfabricated surface-electrode ion trap for scalable quantum information processing. *Phys. Rev. Lett.* **96,** 253003 (2006).
24. Langer, C. *et al.* Long-lived qubit memory using atomic ions. *Phys. Rev. Lett.* **95,** 060502 (2005).
25. Jost, J. D. *et al.* Entangled mechanical oscillators. *Nature* **459,** 683–685 (2009).
26. Campbell, W. C. *et al.* Ultrafast gates for single atomic qubits. *Phys. Rev. Lett.* **105,** 090502 (2010).
27. King, B. E. *et al.* Cooling the collective motion of trapped ions to initialize a quantum register. *Phys. Rev. Lett.* **81,** 1525–1528 (1998).
28. Hayes, D. *et al.* Coherent error suppression in spin-dependent force quantum gates. Preprint at ⟨http://arxiv.org/abs/1104.1347⟩ (2011).
29. Sackett, C. A. *et al.* Experimental entanglement of four particles. *Nature* **404,** 256–259 (2000).
30. Levitt, M. H. Composite pulses. *Prog. Nucl. Magn. Reson. Spectrosc.* **18,** 61–122 (1986).
31. Heinzen, D. J. & Wineland, D. J. Quantum-limited cooling and detection of radio-frequency oscillations by laser-cooled ions. *Phys. Rev. A* **42,** 2977–2994 (1990).
32. Brown, K. R. *et al.* Coupled quantized mechanical oscillators. *Nature* **471,** 196–199 (2011).
33. Harlander, M., Lechner, R., Brownnutt, M., Blatt, R. & Hänsel, W. Trapped-ion antennae for the transmission of quantum information. *Nature* **471,** 200–203 (2011).

Acknowledgements We thank M. J. Biercuk, J. J. Bollinger and A. P. VanDevender for experimental assistance, J. C. Bergquist, C. W. Chou and T. Rosenband for the loan of a fibre laser, R. Jordens and E. Knill for comments on the manuscript, and D. Hanneke and J. P. Home for discussions. We thank P. Treutlein for discussions on microfabrication techniques. This work was supported by IARPA, the ONR, DARPA, the NSA, Sandia National Laboratories and the NIST Quantum Information Program. This paper, a submission of NIST, is not subject to US copyright.

Author Contributions C.O. participated in the design of the experiment and built the experimental apparatus, collected data, analysed results and wrote the manuscript. U.W. participated in building the experimental apparatus, collected data and analysed results. Y.C. developed chip fabrication methods and fabricated the ion trap chip. K.R.B. participated in the design of the experiment, developed chip fabrication methods and helped build parts of the experiment. J.M.A. developed chip fabrication methods and automated experiment control and data taking. D.L. participated in the design of the experiment, collected data and maintained the laser systems. D.J.W. participated in the design and analysis of the experiment. All authors discussed the results and the text of the manuscript.

Author Information Reprints and permissions information is available at www.nature.com/reprints. The authors declare no competing financial interests. Readers are welcome to comment on the online version of this article at www.nature.com/nature. Correspondence and requests for materials should be addressed to C.O. (christian.ospelkaus@iqo.uni-hannover.de).

METHODS

Determination of the local microwave field. Within a small region $\{\delta x, \delta y, \delta z\}$ around the oscillating microwave field null point, we expect $\mathbf{B}_{\mathrm{osc}}$ to be a quadrupole

$$\mathbf{B}_{\mathrm{osc}} = B' \cos(2\pi f_s t) \begin{pmatrix} \cos(2\alpha) & 0 & \sin(2\alpha) \\ 0 & 0 & 0 \\ \sin(2\alpha) & 0 & -\cos(2\alpha) \end{pmatrix} \begin{pmatrix} \delta x \\ \delta y \\ \delta z \end{pmatrix}$$

in the coordinate system of Fig. 1, where B' and α (the angle of one principal axis of the quadrupole with respect to the x direction in Fig. 1) characterize the strength and orientation of the quadrupole, respectively. We map the x–z spatial dependence of the a.c. Zeeman shift on the magnetic dipole transition $|3,1\rangle \rightarrow |2,0\rangle$ by displacing the ion radially from its nominal position with adjustments of the control electrode potentials that are derived from simulations. We determine the a.c. Zeeman shifts for a set of radial displacements $\{\delta x, \delta z\}$ and find that $B' = 35.3(4)\ \mathrm{T\,m^{-1}}$ and $\alpha = 26.6(7)^\circ$ from a fit to this data. As a consistency check, we probe the relevant one-ion sideband with frequency near 6.5 MHz and find a π-time for the ion in its motional ground state of approximately 260 μs (extracted by a model fit). The discrepancy of 27% between the observed π-time and that inferred from the measured gradient is most probably due to a misalignment between the maximal gradient direction and the axis of the interrogated motional mode. (To maintain a reasonable trap depth, the motional mode could not be perfectly overlapped with the maximal gradient.)

Determination of populations from state-dependent fluorescence. During one detection period (duration, 100 μs), we typically detect ~0.3 counts on average if both ions are projected into $|\uparrow\rangle$, and approximately 11 additional counts for each ion in state $|\downarrow\rangle$.

Reference histograms are derived by recording photon counts for an on-resonance Ramsey experiment with two ions where the phase, θ, of the second $\pi/2$-pulse was varied. We establish in independent experiments that the net effect of transferring in and out of the qubit basis, and the Ramsey pulses, gives population errors not exceeding 0.02. We therefore assume the respective probabilities of observing zero, one or two fluorescing ions to be

$$P_0(\theta) = \cos^4(\theta/2)$$
$$P_1(\theta) = \sin^2(\theta)/2$$
$$P_2(\theta) = \sin^4(\theta/2)$$

We model each histogram for two, one or zero fluorescing ions as a sum of three Poisson distributions with variable weights and average counts. The weights and averages are determined by a simultaneous least-squares fit to the experimentally determined histograms for all phases θ. To reduce the number of free parameters, we fix the two-ion average to be twice the one-ion average. With this choice, the fit contains eight free parameters and has a reduced χ^2 value of 1.34. Using the histograms representing two, one and zero fluorescing ions, we do a second least-squares fit to the histograms obtained while scanning the phase, ϕ, of the $\pi/2$-pulse following the entangling gate. Each population is fitted to functions $a_k \cos(2\phi + \phi_0) + a_{0,k}$, where a_k and $a_{0,k}$ ($k = 0$, 1 or 2 fluorescing ions) are pairs of constants and ϕ_0 is a common phase offset. The least-squares fits are shown in Fig. 4a. These fits directly yield the parity amplitude, A_{II}, the phase offset, ϕ_0, and the offset from zero shown in Fig. 4b.

The final uncertainty in the fidelity, F_s, is derived from the uncertainties in the population fits. In addition to the data analysis described above, we apply several other parameterizations of the histograms to fit to the Ramsey reference experiment. In all instances, the resulting gate fidelities agree with our stated result to within the respective uncertainties.